

REMARKS

The Office Action of February 17, 2006 has been received and its contents carefully considered.

Claims 1 to 5 are all the claims pending in the application.

The Examiner advises that he has interpreted the phrase “3d transition metal elements” used throughout the claims to be limited to the elements Cr, Mn, Fe, Co, Ni and Cu as set forth in Paragraph [20] of the specification.

In response, applicants have amended claim 1 to recite the metal elements described in Paragraph [20] of the application.

Claim 1 has been rejected under 35 U.S.C. § 102(b) as anticipated by EP 0 364 631 A1 to Mizumoto et al.

Applicants submit that EP ‘631 does not disclose or render obvious the presently claimed invention and, accordingly, request withdrawal of this rejection.

The present invention as set forth in claim 1 as amended above is directed to a magnetic crystalline alloy comprising Pt in an amount of 40 at% to 60 at%, and at least two 3d transition metal elements selected from the group consisting of Cr, Mn, Fe, Co, Ni, and Cu, wherein the total amount of the 3d transition metal elements is from 60 at% to 40 at%, and the average number of valence electrons in the respective 3d transition metal elements as calculated on the basis of the compositional proportions of the elements is from 7.5 to 8.55.

Thus, applicants have amended claim 1 to recite that the alloy is crystalline, and that the average number of valence electrons in the respective 3d transition metal elements as calculated on the basis of the compositional proportions of the elements is from 7.5 to 8.55.

Support for the amendment to claim 1 to recite the value 8.55 can be found in the present specification at page 13, Table 2, Example 2.

In the Response Under 37 C.F.R. § 1.111 filed on December 2, 2005, applicants pointed out that the average number of valence electrons in the respective 3d transition metal elements of the $\text{Pt}_{46}\text{Ni}_1\text{Co}_{53}$ alloy in Example 3 of EP '631, upon which the Examiner relied, would be calculated to be 9.02.

In the present Office Action, the Examiner states that since the calculated 9.02 value is very similar and closely approximates the claimed upper limit of 9 of original claim 1, one of ordinary skill in the art would have expected the example alloy of EP '631 and the presently claimed alloys to have the same properties.

In response, and as discussed above, applicants have amended claim 1 to recite that the upper limit is 8.55.

Since claim 1 recites that the upper limit be 8.55 and the alloy the Examiner has identified has a value of 9.02, applicants submit that the $\text{Pt}_{46}\text{Ni}_1\text{Co}_{53}$ of EP '631 does not anticipate claim 1.

Further, applicants again point out that technology field is different between the present invention and EP '631. As described in the "Object of the Invention" on page 3 of EP '631, the

invention of EP '631 is basically related to the technology field of a magneto-optical recording media, recently often called "MO", which is totally different from that of the present invention.

The present invention relates to a magnetic alloy for a magnetic layer used in a magnetic recording medium for a so-called "hard disk" device. Accordingly, the characteristics necessary to the present invention are totally different from those of the magneto-optical recording media, and do not need the parameters disclosed in Table 1 on page 9 of EP '631.

In addition, EP '631 discloses that an amorphous alloy is necessary for a magneto-optical recording media. See the entire disclosure of EP '631, including the Title, Field of Invention Object of the Invention, and Summary of the Invention, which indicate that the invention of JP '631 is directed to an amorphous alloy. However, the present invention relates to a magnetic alloy having a crystallized structure, which is obvious to a person having ordinary skill in the art who reads paragraph [25] at page 7 of the present specification describing the order parameter, or the orientation of the crystal such as (001) or (002).

Accordingly, applicants submit that the reasons for the rejection are unfounded.

In particular, applicants submit that the Examiner's statement that Example 3 at page 9 of EP '631, which is an amorphous alloy, anticipates claim 1 of the present application is in error.

With respect to applicants' arguments that the EP '631 alloy is amorphous whereas the alloy of the present invention has a crystalline structure, the Examiner states that he is not persuaded because the present claims are silent with respect to the crystalline structure of the claimed alloy. The Examiner states that the present claims, therefore, encompass the amorphous structure taught by EP '631.

In response, applicants have amended claim 1 to state that the alloys of the present invention are crystalline. Support for this amendment to recite a crystalline structure for the claimed alloy is found in the present specification in its description of the alloy.

For example, paragraph [22] of the present specification states that if the total amount of the 3d transition metal elements exceed 60 at%, “the structure of the magnetic alloy changes $L1_0$ to another structure”. A “ $L1_0$ ” structure refers to a particular crystal structure among the many crystal structures that are known to exist. See the attached Attachment A, which is a compilation of various printouts that were obtained from the following website links: <http://cst-www.nrl.navy.mil/lattice/index.html>; <http://cst-www.nrl.navy.mil/lattice/struk/index.html>; <http://cst-www.nrl.navy.mil/lattice/struk/ltype.html>; and http://cst-www.nrl.navy.mil/lattice/struk/l1_0.html. These printouts describe “Crystal Lattice Structures.”

As can be seen from the enclosed Attachment A, crystal lattice structures can be designated in a variety of different ways, including a “Strukturbericht Designation.” As set forth in Attachment A, Strukturbericht symbols (designations) are a partly systematic method for specifying the structure of a crystal. The L designation is used to describe alloy crystal types, and among the Strukturbericht Type L structures, there is the $L1_0$ (AuCu) structure.

Thus, the reference to the $L1_0$ structure in the present specification clearly shows that the alloys of the present invention are crystalline.

Moreover, in the claims, (001) and (002) refer to a “plane direction”, which is used to describe a crystal structure, and which is never used to describe an amorphous structure. See, for example, Fig. 2 on page 1707 of the attached Attachment B, Le Bouar, Y., “MECHANISM

AND MODELING OF SAW-TOOTH STRUCTURE FORMATION IN THE $L1_2$ - $L1_0$ TWO-PHASE SYSTEM,” Acta mater., Vol. 48 (2000), pages 1705-1717.

EP '631 shows in Example 3 of Table 1 that the $Pt_{46}Ni_1Co_{53}$ alloy is amorphous for its crystalline condition, and its Kerr rotation angle (θ_k) is 0.15 and H_{co} (coercive force) is 0.9 for the magneto-optical characteristics. EP '631 also shows in Example 22 that the alloy $Pt_{75}Co_{25}$ is crystalline for its crystalline condition, but its Kerr rotation angle (θ_k) is unmeasurable, and H_{co} (coercive force) is also unmeasurable. This means that the characteristics or purpose of the amorphous alloy of EP '631 cannot be applied to a crystal alloy.

On the other hand, the magnetic alloy of the present invention has a crystal structure, and does not have the same characteristics as the magneto-optical effects of the alloy of EP '631, such as Kerr rotation angle (θ_k).

In view of the above, applicants submit that EP '631 does not anticipate claim 1 and, accordingly, request withdrawal of this rejection.

Claims 2 and 3 have been rejected under 35 U.S.C. § 102(b) as anticipated by or, in the alternative, under 35 U.S.C. § 103(a) as obvious over EP '631.

The Examiner states that EP '631 is silent with respect to the properties recited in claims 2 and 3. The Examiner argues that the alloy disclosed in EP '631 would be expected to possess all of the same properties as recited in present claims 2 and 3 because the alloy disclosed in EP '631 has a composition that is encompassed by the present claims.

In response, and as discussed above, applicants submit that the alloy of Example 3 of EP '631 would not be expected to possess all of the same properties as recited in claims 2 and 3.

As stated above, the characteristics necessary to the magnetic alloy of the present invention are totally different from that of the magneto-optical recording media of the EP '631, and the magnetic alloy of the present invention do not need the parameters disclosed in the Table 1 on page 9 of EP '631.

In the Response Under 37 C.F.R. § 1.111 filed on December 2, 2005, applicants stated with respect to the "S" value recited in claim 2, that "although it may be possible to calculate the 'S' value for the alloy of the Example 3 of EP '631, such value 'S' will be zero, which has no technical meaning, because of the characteristics of the amorphous alloy."

The Examiner states in the present Office Action that applicants have not provided any evidence to support the assertion that the "S" value of EP '631 is 0.

In response, applicants provide the following clarifying remarks.

In particular, applicants submit since the alloys of EP '631 are amorphous, the "S" value of the alloy of EP '631 cannot be obtained and, therefore, it is meaningless to refer to an "S" value of an amorphous alloy. Amorphous alloys do not possess an "S" value. This can be illustrated by referring to the attached Attachment C containing X-ray diffraction profiles shown in Figs. 1-3, which Mr. Kanazawa, one of the inventors, has provided.

Figs. 1-3 of Attachment C show X-ray diffraction profiles for Fe-Co-Pt alloys. As described in the present invention, the order parameter "S" is calculated from the integration intensity ($I(001)/I(002)$).

In order to calculate S, at the least, the X-ray intensity from the (002) plane needs to be observed, such as in Fig. 1 and Fig. 2 of Attachment C, which means these alloys have a crystal

structure. However, once the structure becomes amorphous, (001) and (002) peaks cannot be observed, as is shown in Fig. 3 of Attachment C. This means that the “S” value cannot be defined for an amorphous alloy, and I(001) cannot be observed. Therefore, the amorphous alloys of EP ‘631 do not possess an “S” value according to claim 2 of the present application.

Further, it is impossible to calculate the Ku value as set forth in claim 3.

In view of the above, applicants submit that EP ‘631 does not disclose or suggest the subject matter of claims 2 and 3 and, accordingly, request withdrawal of this rejection.

Claims 4 and 5 have been rejected under 35 U.S.C. § 103(a) as obvious over EP ‘631.

The Examiner states that EP ‘631 teaches that the alloy of Example 3 can be used as a magnetic memory medium as disclosed at page 8, lines 46-49.

Applicants continue to believe the Examiner intended to refer to page 6, lines 46-49 of EP ‘631, where it is disclosed that the amorphous alloy thin films have an easy axis of magnetization perpendicular to the film face and can be used in such various fields as magnetic recording materials, including vertical magnetic recording films, magnetic bubble memories and magneto-optical recording.

Claims 4 and 5 are dependent claims that depend ultimately from claim 1 or 2.

Accordingly, applicants submit that claims 4 and 5 are patentable for the same reasons as discussed above with respect to claims 1 and 2.

As stated above, the material itself of the present invention having a crystal structure is totally different from that of EP ‘631 having an amorphous structure.

In view of the above, applicants request withdrawal of this rejection.

AMENDMENT UNDER 37 C.F.R. § 1.116
Application No. 10/628,242

ATTORNEY DOCKET NO. Q76966

In view of the above, reconsideration and allowance of this application are now believed to be in order, and such actions are hereby solicited. If any points remain in issue which the Examiner feels may be best resolved through a personal or telephone interview, the Examiner is kindly requested to contact the undersigned at the telephone number listed below.

The USPTO is directed and authorized to charge all required fees, except for the Issue Fee and the Publication Fee, to Deposit Account No. 19-4880. Please also credit any overpayments to said Deposit Account.

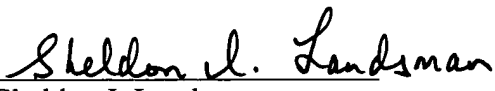
Respectfully submitted,

SUGHRUE MION, PLLC
Telephone: (202) 293-7060
Facsimile: (202) 293-7860

WASHINGTON OFFICE

23373

CUSTOMER NUMBER


Sheldon I. Landsman
Registration No. 25,430

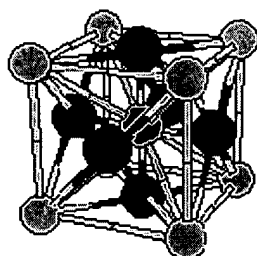
Date: May 17, 2006



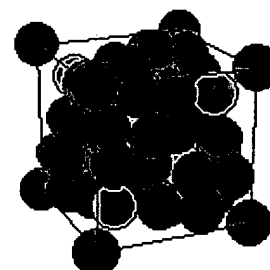
BEST AVAILABLE COPY

Additions to the database? [Read this first.](#)

Questions? [See the FAQ](#)



Crystal Lattice^{*} Structures

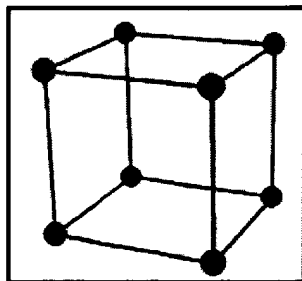


Indexed by	
<i>Strukturbericht</i> Designation	Pearson Symbol
Space Group	Prototype
Structures of Intermetallic Alloy Phases	

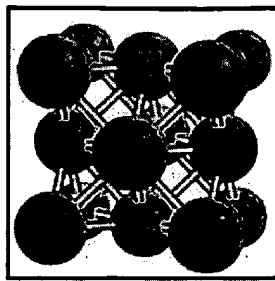
This page offers a concise index of common crystal lattice structures. A graphical representation as well as useful information about the lattices can be obtained by clicking on the desired structure below.

This page currently contains links to 254 structures in 90 of the 230 space groups.

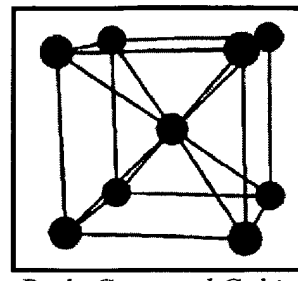
BEST AVAILABLE COPY



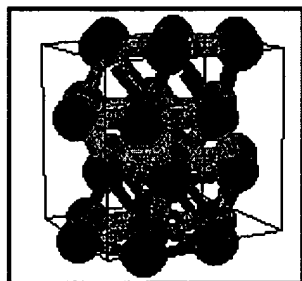
Simple Cubic
and related structures



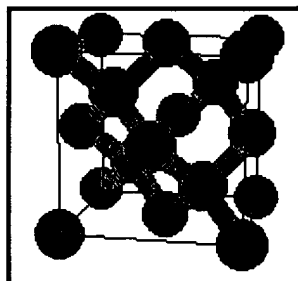
Cubic Close Packed
and related structures



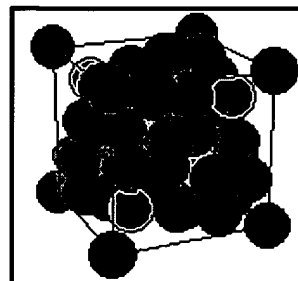
Body Centered Cubic
and related structures



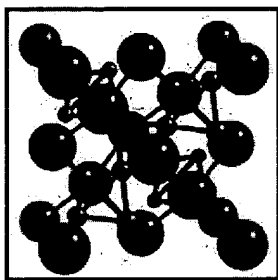
Hexagonal Close Packed
and related structures



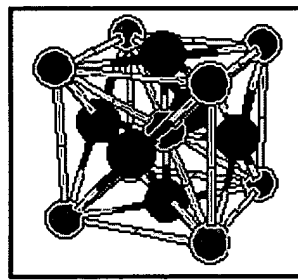
Carbon
and Related Structures



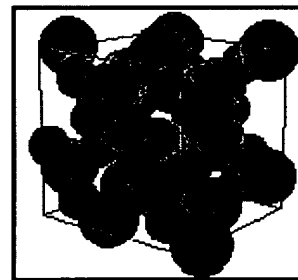
Manganese Structures



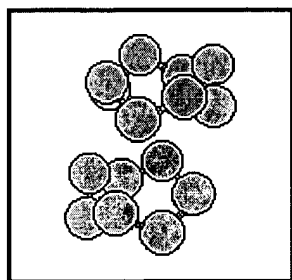
The Laves Phases



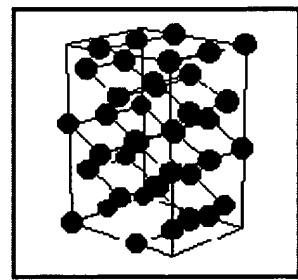
Perovskite
and Related Structures



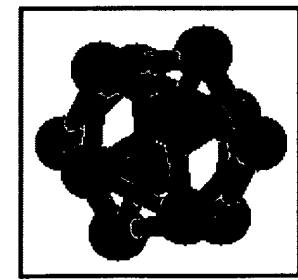
Quartz (SiO_2)
and Related Structures



Sulfur and its Compounds

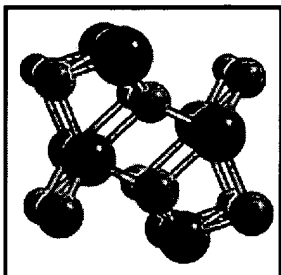
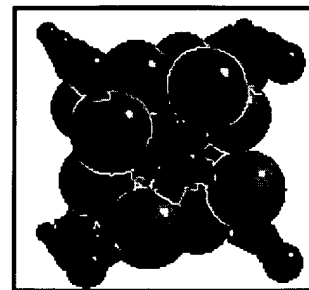


Lanthanides, Actinides,
and Compounds



IIIb-VIIb Elements
and Compounds

BEST AVAILABLE COPY

*Binary Pnma Alloys**Other Structures*

Structures indexed by:

- *Strukturbericht* Designation
- Pearson Symbol
- Space Group
- Prototype

References used in creating these pages.

Programs used in creating these pages.

Other sources of information about crystal lattices can be found at various sites around the Web.

NRL policy prohibits mention of the creators of this page.

Questions, comments, additions, and corrections are welcome, (Privacy Advisory) but first please read the FAQ. If you would like to see a structure added to the database, please read here first.

Return to the Code 6390 Home Page.

This page maintained by lattice@dave.nrl.navy.mil (Privacy Advisory)

Current URL: <http://cst-www.nrl.navy.mil/lattice/index.html>

Last updated: 21 October 2004.

The appearance of external hyperlinks does not constitute endorsement by the United States Department of Defense, the United States Department of the Navy, and the Naval Research

Laboratory of the linked web sites, or the information, products or services contained therein. For other than authorized activities such as military exchanges and Morale, Welfare, and Recreation (MWR) sites, the United States Department of Defense, the Department of the Navy, and the Naval Research Laboratory does not exercise any editorial control over the information you may find at these locations. Such links are provided consistent with the stated purpose of this DoD web site.

[Return to CCMS home page](#)



Crystal Lattice Structures:

Reference Date: 1 Sep 1995

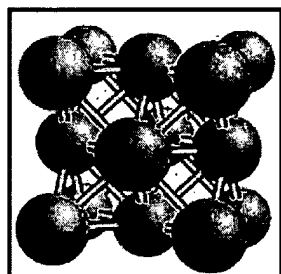
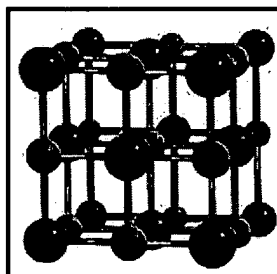
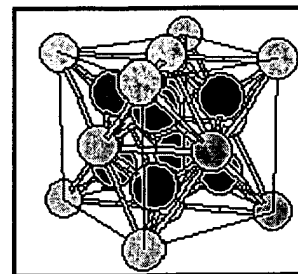
Last Modified: 21 Oct 2004

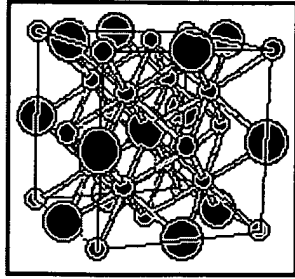
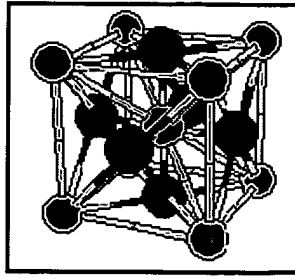
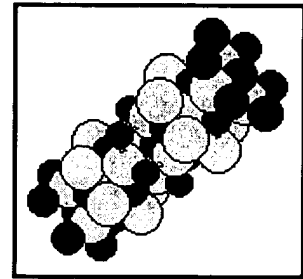
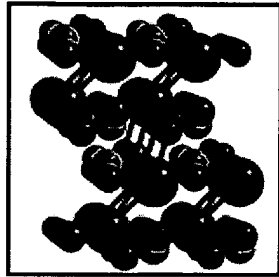
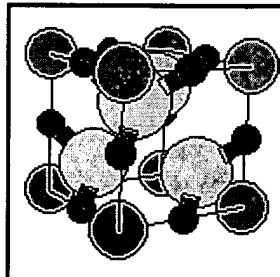
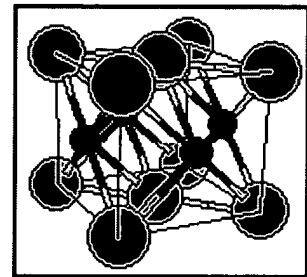
Index by *Strukturbericht* Designation

- *Strukturbericht* symbols are a partly systematic method for specifying the structure of a crystal. Thus the A structures are supposed to be monatomic, B's are diatomic with equal numbers of atoms of each type, C's have a 2-1 abundance ratio, D's are 3-1, etc. Unfortunately, this scheme breaks down as early as A15. Numbers were assigned in roughly the historical order of the study of the lattice.
- Barrett and Massalski give a table (p. 29) which gives the correspondence between the *Strukturbericht* types and the complexity of the crystal:

<i>Strukturbericht</i> Designation	Crystal Type
<u>A</u>	Elements
<u>B</u>	AB compounds
<u>C</u>	AB ₂ compounds
<u>D</u>	A _m B _n compounds
<u>E, F, G, H</u> ... K	More complex compounds
<u>L</u>	Alloys
<u>O</u>	Organic compounds
<u>S</u>	Silicates

Strukturbericht Types:

A TypeB TypeC Type

BEST AVAILABLE COPY**D Type****E Type****F Type****G Type****H Type****L Type**

[Go back to Crystal Lattice Structure page.](#)

Structures indexed by:

- [Pearson Symbol](#)
- [Space Group](#)
- [Prototype](#)

Current URL: <http://cst-www.nrl.navy.mil/lattice/struk/index.html>

*This page was created at the
[Naval Research Laboratory](#)
[Center for Computational Materials Science](#)*

Send comments and corrections to
lattice@dave.nrl.navy.mil (Privacy Advisory)

The appearance of external hyperlinks does not constitute endorsement by the United States Department of Defense, the United States Department of the Navy, and the Naval Research Laboratory of the linked web sites, or the information, products or services contained therein. For other than authorized activities such as military exchanges and Morale, Welfare, and Recreation (MWR) sites, the United States Department of Defense, the Department of the Navy, and the Naval Research Laboratory does not exercise any editorial control over the information you may find at these locations. Such links are provided consistent with the stated purpose of this DoD web site.

[Return to CCMS home page](#)

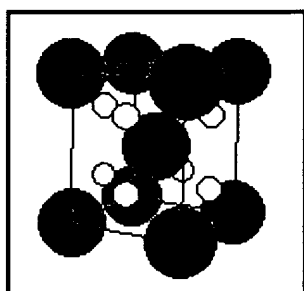


Crystal Lattice Structures:

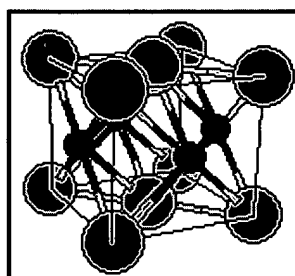
Creation Date: 17 May 2002

Last Modified: 21 Oct 2004

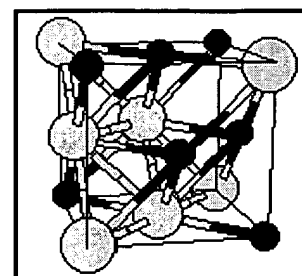
Strukturbericht Type L



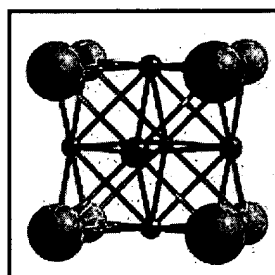
L'2 (ThH₂) Structure



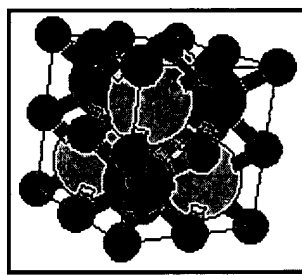
L1₀ (AuCu) Structure



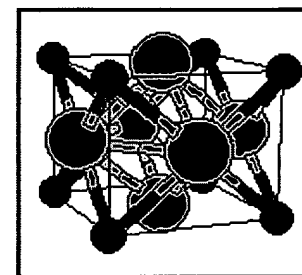
L1₁ (CuPt) Structure



L1₂ (Cu₃Au) Structure



L2₁ (Heusler) (AlCu₂Mn)
Structure



L6₀ (CuTi₃) Structure

[Go back to the Strukturbericht home page](#)

[Go back to Crystal Lattice Structure page.](#)

Structures indexed by:

- [Pearson Symbol](#)
- [Space Group](#)
- [Prototype](#)

Current URL: <http://cst-www.nrl.navy.mil/lattice/struk/ltype.html>

*This page was created at the
Naval Research Laboratory
Center for Computational Materials Science*

Send comments and corrections to
lattice@dave.nrl.navy.mil (Privacy Advisory)

The appearance of external hyperlinks does not constitute endorsement by the United States Department of Defense, the United States Department of the Navy, and the Naval Research Laboratory of the linked web sites, or the information, products or services contained therein. For other than authorized activities such as military exchanges and Morale, Welfare, and Recreation (MWR) sites, the United States Department of Defense, the Department of the Navy, and the Naval Research Laboratory does not exercise any editorial control over the information you may find at these locations. Such links are provided consistent with the stated purpose of this DoD web site.

[Return to CCMS home page](#)

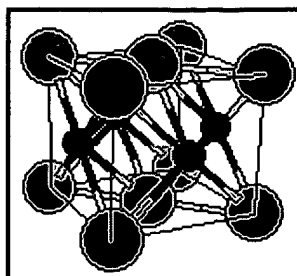


Crystal Lattice Structures:

Reference Date: 5 August 1997

Last Modified: 21 Oct 2004

The CuAu (L1₀) Structure



You can now

- [see the structure from several perspectives](#);
- [examine the structure with an external viewer](#); or
- [download the coordinates of the atoms in these pictures in XYZ format](#).
- [visualize the structure](#) (Uses the [JMOL Applet](#))

-
- This is a tetragonal distortion of the fcc structure. The atoms are at the positions of a [face centered cubic](#) lattice when $c = a$. [Indium \(A6\)](#) has a related structure. The [B19 \(AuCd\)](#) structure reduces to L1₀ in certain cases, as does the [L6₀ \(CuTi₃\)](#) structure.
 - Note that Pearson's Handbook sometimes assigns a Pearson symbol of tP4, rather than tP2. Since Pearson's Handbook also says [CuTi₃](#) is in the CuAu structure, I'll use my best judgment.
-

- Prototype: AuCu
- Pearson Symbol: [tP2](#)
- *Strukturbericht* Designation: [L1₀](#)
- Space Group: [P4/mmm](#) ([Cartesian](#) and [lattice coordinate](#) listings available)
- Number: [123](#)
- Other Compounds with this Structure: [TiAl](#), [NiIn](#)
- Primitive Vectors:

$$\mathbf{A}_1 = \frac{1}{2} a \mathbf{X} - \frac{1}{2} a \mathbf{Y}$$

$$\mathbf{A}_2 = \frac{1}{2} a \mathbf{X} + \frac{1}{2} a \mathbf{Y}$$

$$\mathbf{A}_3 = c \mathbf{Z}$$
- Basis Vectors:

$$\mathbf{B}_1 = 0 \quad (\text{Au}) \quad (1a)$$

$$\mathbf{B}_2 = \frac{1}{2} \mathbf{A}_1 + \frac{1}{2} \mathbf{A}_2 + \frac{1}{2} \mathbf{A}_3 = \frac{1}{2} a \mathbf{X} + \frac{1}{2} c \mathbf{Z} \quad (\text{Cu}) \quad (1d)$$

See these vectors in LaTeX output format.

[Go back to the Cubic Close Packed Structure page.](#)

[Go back to Crystal Lattice Structure page.](#)

Structures indexed by:

- [Strukturbericht Symbol](#)
- [Pearson Symbol](#)
- [Space Group](#)
- [Prototype](#)

Current URL: http://cst-www.nrl.navy.mil/lattice/struk/l1_0.html

*This page was created at the
Naval Research Laboratory
Center for Computational Materials Science*

Send comments and corrections to
lattice@dave.nrl.navy.mil ([Privacy Advisory](#))

The appearance of external hyperlinks does not constitute endorsement by the United States Department of Defense, the United States Department of the Navy, and the Naval Research Laboratory of the linked web sites, or the information, products or services contained therein. For other than authorized activities such as military exchanges and Morale, Welfare, and Recreation (MWR) sites, the United States Department of Defense, the Department of the Navy, and the Naval Research Laboratory does not exercise any editorial control over the information you may find at these locations. Such links are provided consistent with the stated purpose of this DoD web site.

[Return to CCMS home page](#)



PERGAMON

Acta mater. 48 (2000) 1705–1717



www.elsevier.com/locate/actamat

MECHANISM AND MODELING OF SAW-TOOTH STRUCTURE FORMATION IN THE L_{12} - L_{10} TWO-PHASE SYSTEM

Y. LE BOUAR^{1,2} and A. G. KHACHATURYAN[†]

¹Department of Ceramic and Materials Engineering, Rutgers University, Piscataway, NJ 08855-0909, USA and ²Laboratoire d'Etude des Microstructures, CNRS-ONERA, B.P. 72, 92322, Châtillon, Cedex, France

(Received 9 September 1999; accepted 23 December 1999)

Abstract—The strain-accommodating mechanism of formation of the saw-tooth microstructure in the $L_{12}+L_{10}$ two-phase ordered system is proposed. To describe the atomic scale kinetics of ordering and decomposition in this system, the master equation, which explicitly incorporates the effect of the transformation strain, is formulated. It is used to simulate the precipitation of the L_{10} phase from the L_{12} parent phase in the Co–Pt alloy. The computer simulation shows that the decomposition occurs heterogeneously on antiphase boundaries of the L_{12} structure if the composition is near the solubility limit of the L_{12} phase. It eventually produces the saw-tooth microstructure. The decomposition transforms the (010) antiphase boundary into a layer of the single-variant tetragonal L_{10} phase separating the L_{12} antiphase domains. Later, the strain accommodation transforms this single-variant L_{10} phase layer into the saw-tooth pattern. The simulation results are in excellent qualitative and quantitative agreement with our TEM images of $\text{Co}_{38.5}\text{Pt}_{61.5}$. © 2000 Acta Metallurgica Inc. Published by Elsevier Science Ltd. All rights reserved.

Keywords: Phase transformations; Microstructure; Elastic properties; Theory & modeling; Alloys

1. INTRODUCTION

TEM observations of the decomposition in Co–Pt alloys [1, 2] have shown that the two-phase microstructure in these alloys forms a very unusual saw-tooth-like morphology. This morphology has been reported in Refs [1, 2] for the $\text{Co}_{38.5}\text{Pt}_{61.5}$ alloy, gradually cooled to 873 K. At 873 K, this alloy is in an $L_{12}+L_{10}$ two-phase state with a small volume fraction of the L_{10} phase. As shown in Ref. [2], the cooling initially produces large L_{12} antiphase domains separated by thin single-domain layers of the L_{10} phase. These layers are smooth as long as their width does not exceed about 3–4 nm. When the width exceeds this critical thickness, the layers become unstable and suddenly adopt a saw-tooth-like shape (see Fig. 1).

Co–Pt alloys are not the only type of system where the saw-tooth structure is observed; it was also observed in Cu–Be alloys by Cheong *et al.* [3]. The structure is formed during the decomposition of a hyper-eutectoid β (b.c.c.) phase producing the $\gamma(\text{B2})+\alpha(\text{f.c.c.})$ two-phase mixture. The crystallography and kinetics of the decomposition reaction

here is much more complex than in the $\text{Co}_{38.5}\text{Pt}_{61.5}$ alloy. The decomposition in the Cu–Be alloy is accompanied by the $\text{B2} \rightarrow \text{f.c.c.}$ crystal lattice rearrangement described by the tetragonal Bain distortion. The common feature of these two very different systems is that the parent phase is ordered and that the stress-free transformation strain is tetragonal. This circumstance hints that in both cases the saw-tooth microstructure is caused by the transformation-induced strain and somehow related to the ordered character of the parent phase.

The first step towards understanding the mechanism of the saw-tooth microstructures has been made by analyzing the dark field and high resolution electron microscope images of the Co–Pt alloys [2]. It has been shown that the L_{12} phase has no antiphase boundaries: the antiphase L_{12} domains are always separated by an L_{10} phase layer. This is in agreement with the prediction that the absence of the antiphase boundaries (APBs) in an ordered system is an indication that the ordered phase is formed within the two-phase field of the phase diagram [4]. It has also been shown that the tetragonal axis of the L_{10} layer is always normal to the antiphase vector relating the two L_{12} domains [1, 2].

A detailed mean field study [1, 5] of the APB-

[†] To whom all correspondence should be addressed..

enhanced precipitation of the $L1_0$ ordered phase has shown that the nearest and next-nearest interaction is sufficient to explain both the formation of the $L1_0$ layer on the APBs and the relationship between the directions of the tetragonal axis and antiphase shift vectors. However, this short-range interaction model is unable to explain the formation of the saw-tooth morphology. The purpose of this paper is twofold. We developed the kinetic model that incorporates the strain energy into the thermodynamics and kinetics of the coherent decomposition so that the model is applicable irrespective of the geometrical complexity of the microstructure pattern. Using this model, we reveal the mechanism of formation of the saw-tooth structure. It will be shown that:

1. if the alloy composition is in a vicinity of the ordered phase solved on the phase diagram, the precipitation of the second phase mainly occurs on antiphase boundaries;
2. the saw-tooth morphology develops as a result of a relaxation of the long-range coherency strain.

2. THEORETICAL MODEL

The crystal lattice misfit between the cubic $L1_2$ and tetragonal $L1_0$ phases is described by the tetragonal stress-free transformation strain tensor. The $L1_0$ phase forms three tetragonal orientation variants in the f.c.c. structure whose unit cells are shown at the top of Fig. 1(a). Each variant generates its own stress-free tensor. These tensors are related by the symmetry operations of the parent f.c.c. phase. The misfit between lattices of the orien-

tation variants and parent phase generates the elastic displacements and related elastic strain. The strain energy caused by the phase transformation is stored in the strain field. Unlike the chemical free energy that depends only on the volume of the phases, the strain energy also depends on the shape and spatial pattern formed by the $L1_0$ phase precipitates. Under these conditions, the strain energy is affected by the geometry of the microstructure pattern and thus controls the two-phase microstructure evolution. This coherency strain is a quite common phenomenon for practically all multiphase coherent systems. Therefore, any realistic theory of the microstructure evolution should take the transformation-induced strain into account.

In systems such as alloys with the $L1_0 + L1_2$ two-phase field, the strain should be explicitly incorporated into the thermodynamics and kinetics of the phase transformation. One of the most impressive examples illustrating the influence of the strain-induced interactions is a formation of the chessboard-like microstructures during a precipitation of a tetragonal phase from the cubic parent phase. The chessboard-like microstructures have been observed in many systems such as Co-Pt [1, 2] and CuAu-Pt [6]. The theory of the chessboard structures was developed by Le Bouar *et al.* [7]. The computer simulation in [7] has demonstrated that the chessboard structure is formed as a result of the strain-induced microstructure evolution in the cubic \rightarrow cubic + tetragonal transformation.

The transformation-induced strain is also a key factor in developing the saw-tooth structure. Special conditions under which the saw-tooth structure is formed are actually revealed by the TEM observations [1]. According to these observations, the saw-tooth structure is formed on the APBs within the $L1_2$ ordered phase. To describe the processes developing on the APBs, the kinetic theory should be microscopic. There are two microscopic kinetic theories that can be used. One of these theories, formulated in [8, 9], is applicable to the case of small transformation driving force, i.e. when the system is not too far from equilibrium (when the supersaturation is small): the evolution rate is assumed to be a linear function of the thermodynamic driving force. In particular, this approach is applicable for the coarsening regime. The microscopic theory [8, 9] has been extended in [10] by including the strain energy. The second approach to this problem is based on the kinetic master equation (ME). Although the ME approach is more complicated, its applicability can be extended to a regime where the transformation driving force is high. This is a high supersaturation regime of the growth stage. In the latter case, a mean field approximation of the ME results in a set of coupled kinetic equations describing the evolution of the occupation probabilities and multiparticle correlation functions, the



Fig. 1. Dark field image of the $\text{Co}_{38.5}\text{Pt}_{61.5}$ alloys gradually cooled from 1023 to 873 K at the rate of 40 K, aged for 15 days at 873 K and water quenched. The dark field image was obtained in a zone axis close to (001) with the superstructure reflection (210).

evolution rate a non-linear function of the thermodynamic driving force.

2.1. Kinetic equation

A new and very effective method of using the ME for the nearest-neighbor jump diffusion in a binary substitutional alloy has been developed in Refs [11, 12]. The method uses an approximation based on decoupling the averages of products of occupation numbers $c(r)$ related to different crystal lattice sites [$c(r)$ is a value equal to 1 if the site r is occupied by solute atom and 0 otherwise]. This decoupling procedure results in the mean field approximation, which drastically simplifies the ME and makes it a convenient tool for the description of the microscopic kinetics far from equilibrium.

If the mixing energies are assumed to be pairwise, the corresponding ME equation is

$$\frac{\partial n(r)}{\partial t} = \sum_{r'} L(r-r') \left\{ (1 - n(r))n(r')e^{\beta \frac{(\Phi(r')) - (\Phi(r))}{2}} - n(r)(1 - n(r'))e^{\beta \frac{(\Phi(r)) - (\Phi(r'))}{2}} \right\} \quad (1)$$

where $\beta = 1/k_B T$, k_B is the Boltzmann constant,

$$\langle \Phi(r) \rangle = \sum_{r'' \neq r} W(r-r'') n(r'') \quad (2)$$

is the average local potential at the site r caused by the "chemical" short-range interaction with all atoms around the site r , and $W(r-r'')$ is the mixing energy of a pair of atoms in the sites r and r'' . The sum in equation (2) is taken over all r'' sites of the lattice except r . In equation (1), $L(r-r')$ are the transition rate coefficients defined as

$$L(r-r') = \begin{cases} f_0 e^{-\beta U} & \text{if } |r-r'| = a \\ -zf_0 e^{-\beta U} & \text{if } r=r' \\ 0 & \text{otherwise} \end{cases} \quad (3)$$

where f_0 is the frequency of "attempts" of a diffusion jump, U is the diffusion barrier, a is the nearest-neighbor distance and z is the coordination number.

Following Ref. [13], the kinetic equation (2) can be presented as

$$\frac{\partial n(r)}{\partial t} = 2 \sum_{r'} L(r-r') \left\{ (1 - n(r))n(r')n(r) \right. \\ \left. (1 - n(r')) \right\}^{1/2} \sinh \left\{ \beta \frac{\mu(r') - \mu(r)}{2} \right\} \quad (4)$$

where $\mu(r) = \langle \Phi(r) \rangle + \beta^{-1} \ln(n(r)/[1 - n(r)])$ is in

fact the chemical potential $\delta F/\delta n(r)$ calculated from the mean field free energy of the non-equilibrium state:

$$F = F_0 + \sum_{r \neq r'} W(r-r') n(r)n(r') \\ - \beta^{-1} \sum_r n(r) \ln(n(r)) + (1 - n(r)) \ln(1 - n(r)) \quad (5)$$

2.2. Occupation probabilities and the l.r.o. parameters

The system that we investigated consists of phases formed by ordering over f.c.c. lattice sites and decomposition into ordered cubic $L1_2$ (Cu_3Au type) and tetragonal $L1_0$ structure (CuAu type) phases. The preferred positions of the solute and solvent atoms in unit cells of the $L1_2$ phase and in three orientation variants of the $L1_0$ phases are shown in Fig. 2. Occupation probabilities $n(r)$ of both ordered phases and their translational and orientation variants are described by the same equation:

$$n(r) = \bar{c} + \eta_1 \exp(ik_1 r) + \eta_2 \exp(ik_2 r) \\ + \eta_3 \exp(ik_3 r) \quad (6)$$

where \bar{c} is the average composition of the alloy, $r = a_0(x, y, z)$ is the f.c.c. lattice site vector, a_0 is the

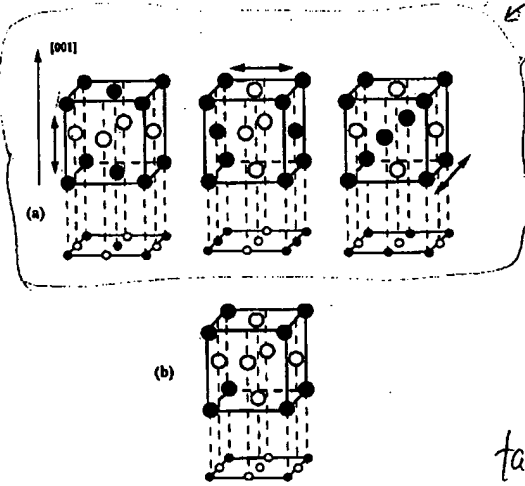


Fig. 2. Unit cells of the $L1_0$ and $L1_2$ structures and their projection on the (001) f.c.c. plane. (a) Unit cells of three variants of the $L1_0$ ordered structure. (b) A unit cell of the $L1_2$ ordered structure. Black circles indicate the solute B atoms, open circles indicate solvent A atoms. Bold lines describe a unit cell. Dashed vertical lines show the projections of alternating columns of B and A atoms along the [001] direction on the (001) plane. Intersection of columns with the (001) plane forms the 2D square lattice. Small black and open circles in sites of the 2D square lattice characterize a type of the columns.

face centered
cubic

f.c.c. lattice parameter, (x, y, z) are coordinates of the f.c.c. lattice sites (x, y, z are integer or half-integers and $x + y + z = \text{integer}$); $\mathbf{k}_1 = 2\pi/a_0(100)$, $\mathbf{k}_2 = 2\pi/a_0(010)$ and $\mathbf{k}_3 = 2\pi/a_0(001)$ are the wave vectors belonging to the same star of the superlattice vectors $\{100\}$; η_1, η_2, η_3 are the components of the l.r.o. parameter. Equation (6) provides a relation between the microscopic parameters, \bar{c} , l.r.o. parameters η_1, η_2, η_3 , and the microscopic parameters, which are the occupation probabilities $n(\mathbf{r})$.

Equation (6) describes the occupation probabilities as a superposition of three concentration waves with the wave vectors, $\mathbf{k}_1, \mathbf{k}_2, \mathbf{k}_3$ [9, 14]. The components η_1, η_2, η_3 of the l.r.o. parameter are amplitudes of three concentration waves. As follows from (6), if $\eta_1 = \eta_2 = \eta_3 = 0$, equation (6) describes a disordered state since all the sites are occupied with the same probability \bar{c} . Otherwise, equation (6) describes an ordered phase.

Depending on the composition \bar{c} , the interatomic interactions in the relevant system are such that the global minimum of the free energy $F(\bar{c}, \eta_1, \eta_2, \eta_3)$ is degenerated and falls at either of six points $\{\eta_1, \eta_2, \eta_3\} = \{\eta, 0, 0\} = \pm\eta(1, 0, 0), \pm\eta(0, 1, 0), \pm\eta(0, 0, 1)$ or at four points $\{\eta_1, \eta_2, \eta_3\} = \{\eta, \eta, \eta\} = \eta(1, 1, 1), \eta(1, \bar{1}, \bar{1}), \eta(\bar{1}, \bar{1}, 1)$ and $\eta(\bar{1}, \bar{1}, \bar{1})$. This degeneracy of the global minimum automatically follows from the symmetry of the free energy $F(\bar{c}, \eta_1, \eta_2, \eta_3)$ with respect to the symmetry operations of the f.c.c. lattice.

Each of six degenerate points $\{\eta, 0, 0\}$, being substituted in equation (6), describes one of six possible $L1_0$ orientation and translation variants. The $L1_0$ structure (see Fig. 2) is formed by alternating cubic planes filled by constituent components. The tetragonal axis of each variant of this structure is parallel to the wave vector of the wave with the non-zero amplitude. Each of four degenerate points $\{\eta, \eta, \eta\}$, being substituted in equation (6), describes one of four translation variants (antiphase domains) of the $L1_2$ phase. Geometrically these antiphase domains are separated by three kinds of APB, each of them being characterized by the antiphase shift vectors, $\mathbf{R}_1 = \frac{1}{2}[011]$, $\mathbf{R}_2 = \frac{1}{2}[101]$ or $\mathbf{R}_3 = \frac{1}{2}[110]$. Because the concentration wave representation (6) is valid for all variants and all compositions of both phases, $L1_2$ and $L1_0$, this approach is well suited for a characterization of the $L1_2 \rightarrow L1_2 + L1_0$ decomposition and, in particular, it is valid for a characterization of decomposition in Co-Pt.

Equation (6) is applicable not only to describe a structurally homogeneous phase, but it is also valid to describe a structurally and compositionally inhomogeneous mesoscopic microstructure with the $L1_2$ and $L1_0$ ordering. In this case, the concentration, $\bar{c}(\mathbf{r})$, and three l.r.o. parameters, $\eta_1(\mathbf{r}), \eta_2(\mathbf{r}), \eta_3(\mathbf{r})$, are "smooth" functions of the coordinate \mathbf{r} rather than constants. The term "smooth" implies that these functions appreciably change over the distances, considerably exceeding the crystal lattice

parameter. The atomic-scale structure of inhomogeneous mesoscopic microstructure is still described by equation (6) using $\bar{c} = \bar{c}(\mathbf{r})$, $\eta_1 = \eta_1(\mathbf{r})$, $\eta_2 = \eta_2(\mathbf{r})$, $\eta_3 = \eta_3(\mathbf{r})$ for each site \mathbf{r} . The mesoscale l.r.o. parameter profiles $\eta_p(\mathbf{r})$ and the composition profile $\bar{c}(\mathbf{r})$ can also be, in turn, expressed through the microscopic parameters, occupation probabilities $n(\mathbf{r})$, by using the equations

$$\eta_p(\mathbf{r}) = \frac{1}{4} \sum_{j=1}^4 n(\mathbf{r} + \mathbf{a}_j) \exp(-i\mathbf{k}_p \cdot \mathbf{a}_j) \quad (7a)$$

$$\bar{c}(\mathbf{r}) = \frac{1}{4} \sum_{j=1}^4 n(\mathbf{r} + \mathbf{a}_j) \quad (7b)$$

where the summation is carried out over the tetrahedron of the nearest neighbors in the f.c.c. lattice, the site \mathbf{r} being its origin. In (7), $\mathbf{a}_1 = 0$ and three vectors, $\mathbf{a}_2, \mathbf{a}_3$ and \mathbf{a}_4 , determine the three nearest-neighbor sites of the f.c.c. lattice tetrahedron with the origin at \mathbf{r} . The vectors \mathbf{k}_p are three superlattice vectors defined in equation (6). Therefore, equations (6) and (7) provide a relation between the mesoscopic and microscopic scales of the inhomogeneous microstructure.

2.3. Strain energy of the structurally inhomogeneous coherent system

No realistic theoretical characterization of a coherent structural transformation is possible unless the transformation-induced elastic strain is taken into account. The strain is generated by the crystal lattice mismatch between the low symmetry phase and the high symmetry matrix, as well as between different orientation variants of the low symmetry phase. The interaction between finite elements of the precipitate phase caused by the strain has a dipole-like long-range asymptotic behavior, which drastically distinguishes it from the short-range "chemical" mixing energies. Because this is the long-distance part of the strain-induced interaction potentials that affects the microstructure evolution, we can use the continuum elasticity for its description. In fact, the potential calculated by using the continuum elasticity is a long-range asymptote of the atomistic potential.

It is important that using the continuum approximation does not introduce an inaccuracy in the description of the morphology evolution. Indeed, the atomistic corrections to the continuum elasticity potentials caused by the discrete nature of a crystal, by definition, are substantial at distances commensurate with interatomic distances and thus are short ranged. Therefore, these atomistic corrections can be incorporated into the short-range "chemical" interaction potentials. As a result, the short-range energies of mixing, W_i , entering (5) become renor-

malized effective mixing energies. They include the short-range atomistic corrections to the continuum elasticity potential. This procedure, in effect, eliminates all inaccuracy in the use of the continuum elasticity instead of crystal lattice statics because in this approach all corrections to the continuum elasticity prove to be incorporated in the mixing energies W_i , which are fitting parameters anyway. They are determined by fitting the calculated phase diagram to the observed one.

The remaining strain interaction potentials are described in terms of the continuum elasticity. These potentials are calculated below by using the Khachaturyan-Shatalov (KS) Phase Field Microelasticity theory of structurally inhomogeneous systems [9, 15]. The total free energy of the system is a sum of the "chemical" free energy (5) (it also includes the short-range corrections to the continuum elasticity) and the elastic energy, i.e. $F = F_{ch} + E_{el}$.

The KS theory provides the analytical solution of the elasticity problem for a body that is macroscopically homogeneous but structurally inhomogeneous in the mesoscopic scale. This is a situation where the typical inhomogeneity length is much smaller than the size of the body. In particular, the KS Phase Field Microelasticity theory gives the closed analytical equation for the strain energy function of the continuous concentration and l.r.o. profiles (phase fields), characterizing an arbitrary coherent microstructure. Using this analytical solution makes it unnecessary to calculate a numerical solution of the elasticity equation for each time increment of the microstructure evolution. This drastically shortens the numerical calculations and allows one to address the problems which are intractable or very time consuming if the finite element methods are used. The KS theory was initially applied to particular step-like phase fields describing structurally homogeneous coherent inclusions with sharp boundaries. The theory has been developed further by Chen *et al.* [16], Wang *et al.* [17] and Le Bouar *et al.* [7], who applied this formalism to the cases of arbitrary continuous phase fields, the concentration and l.r.o. order parameter fields.

In the case where the strain is predominantly caused by the l.r.o. parameter heterogeneities, the stress-free strain ϵ_{ij}^0 determining the crystal lattice misfit at a point r can be presented as a function of η_1, η_2 and η_3 : $\epsilon_{ij}^0 = \epsilon_{ij}^0(\eta_1, \eta_2, \eta_3)$. The stress-free strain is invariant with respect to rigid-body translations which produce the transformations of the l.r.o. parameters:

$$\begin{aligned} (\eta_1, \eta_2, \eta_3) &\rightarrow (\eta_1, -\eta_2, -\eta_3), \\ (\eta_1, \eta_2, \eta_3) &\rightarrow (-\eta_1, \eta_2, -\eta_3), \quad (\eta_1, \eta_2, \eta_3) \rightarrow (-\eta_1, -\eta_2, \eta_3). \end{aligned} \quad (8)$$

Expanding $\epsilon_{ij}^0(\eta_1, \eta_2, \eta_3)$ in the Taylor series up to the first non-vanishing terms and eliminating the expansion terms that are not invariant with respect to the transformations (8) leaves us with an equation which is invariant with respect to any rigid-body translations. The general form of the first non-vanishing term of such an expansion is:

$$\epsilon_{ij}^0(r) = \sum_{p=1}^{p=m} \epsilon_{ij}^{00}(p) \eta_p^2(r) \quad (9)$$

where the tensor $\epsilon_{ij}^{00}(p)$ is the strain transforming the crystal lattice parameters of the f.c.c. phase into the parameters of the equilibrium p th variant of the low symmetry phase, and m is the total number of variants.

In the case of an $L1_2 \rightarrow L1_0$ transformation, the number of possible orientation variants is $m = 3$ and the stress-free strain (9) can be presented as:

$$\begin{aligned} \epsilon_{ij}^0 &= \frac{\eta_1^2}{\eta_0^2} \begin{pmatrix} \epsilon_3 & 0 & 0 \\ 0 & \epsilon_1 & 0 \\ 0 & 0 & \epsilon_1 \end{pmatrix} + \frac{\eta_2^2}{\eta_0^2} \begin{pmatrix} \epsilon_1 & 0 & 0 \\ 0 & \epsilon_3 & 0 \\ 0 & 0 & \epsilon_1 \end{pmatrix} \\ &+ \frac{\eta_3^2}{\eta_0^2} \begin{pmatrix} \epsilon_1 & 0 & 0 \\ 0 & \epsilon_1 & 0 \\ 0 & 0 & \epsilon_3 \end{pmatrix} \end{aligned} \quad (10)$$

where $\epsilon_3 = (c - a_0)/a_0$, $\epsilon_1 = (a - a_0)/a_0$, a_0 and (a, c) are the crystal lattice parameters of the cubic f.c.c. and the tetragonal $L1_0$ phases, and η_0 is the equilibrium l.r.o. parameter of the $L1_0$ phase.

Following Ref. [16], we can express the strain energy as a functional of the l.r.o. fields:

$$E_{elast} = \frac{1}{2} \sum_{p=1}^3 \sum_{q=1}^3 \int \frac{d^3k}{(2\pi)^3} B_{pq} \left(\frac{k}{k} \right) (\eta_p^2(r)) (\eta_q^2(r))^* \quad (11)$$

where $(\eta_p^2(r))_k$ is the Fourier transform of $\eta_p^2(r)$, $(\eta_p^2(r))^*_k$ is the complex conjugate of $(\eta_p^2(r))_k$ and $B_{pq}(e) = C_{ijkl} \epsilon_{ij}^{00}(p) \epsilon_{kl}^{00}(q) - e_i \sigma_{ij}^0(p) \Omega_{jk}(e) \sigma_{kl}^0(q) e_l$, $e = k/k$ is a unit vector in the reciprocal space and e_i its i th component, C_{ijkl} is the elastic moduli tensor, $\sigma_{ij}^0(p) = C_{ijkl} \epsilon_{kl}^{00}(p)$, and $\Omega_{ij}(e)$ is a Green function tensor which is inverse to the tensor $\Omega_{ij}^{-1} = C_{ijkl} e_k e_l$. The integration has to be carried out over the first Brillouin zone, where a volume of $(2\pi)^3/V$ about $k=0$ is excluded from the integration. When the volume V is large, this defines the principal value of the integral.

To make ME equation (1) suitable for characterization of the transformation producing the coherency strain, we have to modify the local potential $\langle \Phi(r) \rangle$ by adding to it the contribution $\langle \Phi(r)_{el} \rangle$ generated by the strain. The latter transforms equation (2) into:

$$\langle \Phi(r) \rangle = \sum_{r''} W(r - r'') n(r'') + \langle \Phi_{el}(r) \rangle \quad (12)$$

where $\langle \Phi(r)_{el} \rangle$ is the variational derivative of (11) in $n(r)$. It can be rewritten as:

$$\begin{aligned} \langle \Phi_{el}(r) \rangle &= \frac{\delta E_{elast}}{\delta n(r)} \\ &= \frac{1}{2} \sum_{p=1}^3 \sum_{q=1}^3 \sum_{j=1}^4 \eta_p(r - a_j) e^{-ik \cdot a_j} \\ &\quad \times \int B_{pq} \left(\frac{k}{k} \right) (\eta_q^2(r))_k e^{ik \cdot (r - a_j)} \frac{d^3 k}{(2\pi)^3}, \quad (13) \end{aligned}$$

where the vectors k_p are the three superlattice vectors defined in equation (6) and the vectors a_j are defined in equation (7).

For numerical calculations it is convenient to express the integrals over k , as sums over all N vectors k within the first Brillouin zone are permitted by the periodical boundary conditions. This gives:

$$\begin{aligned} \langle \Phi_{el}(r) \rangle &= \frac{\delta E_{elast}}{\delta n(r)} \\ &= \frac{1}{2} \sum_{p=1}^3 \sum_{q=1}^3 \sum_{j=1}^4 \eta_p(r - a_j) e^{-ik \cdot a_j} \\ &\quad \times \frac{v}{N} \sum_k' B_{pq} \left(\frac{k}{k} \right) (\eta_q^2(r))_k e^{ik \cdot (r - a_j)} \quad (14) \end{aligned}$$

where $v = a_0^3/4$ is the volume per f.c.c. lattice site, N is the total number of the f.c.c. lattice sites, the prime sign means that the term $k=0$ is excluded from the summation,

$$(\eta_p^2(r))_k = \sum_r \eta_p^2(r) \exp(ik \cdot r). \quad (15)$$

This transition from integration to summation in equation (15) and (16) has the macroscopic accuracy of the order of $1/N$.

The driving force (14) is a functional of the l.r.o. parameters $\eta_p(r)$. Using equation (7) in (14), we express the ME (1) in terms of the function $n(r)$. The obtained kinetic equation with respect to $n(r, t)$ is the nonlinear finite-difference differential equation whose solution fully describes the microscopic and mesoscopic microstructure. Computer simulation of the microstructure evolution is reduced to the numerical solution of this equation.

3. HETEROGENEOUS DECOMPOSITION NEAR ANTIPHASE BOUNDARIES

To insure that the free energy (5) provides the phase diagram with the $L1_2 + L1_0$ two-phase field, a proper interaction model has to be chosen. The simplest short-range interaction model which results in the $L1_2 + L1_0$ two-phase concentration range is the nearest and next-nearest interaction model, with the positive nearest-neighbor mixing energy W_1 and negative next-nearest energy W_2 . In this work we

consider the case $W_2/W_1 = -0.2$, $W_1 > 0$. At the temperature $T = 1.125W_1/k_B$, the calculated $L1_2 + L1_0$ two-phase field is within the range $0.42 < c < 0.43$ at this temperature. This range is of the same order as the observed $L1_2 + L1_0$ two-phase range in the prototype Co-Pt system (approximately $0.395 < c_{Co} < 0.405$ at 963 K, Ref. [2]).

3.1. Short-range interaction

The formation of the saw-tooth structures is observed on the APBs of the $L1_2$ phase, which were almost perpendicular to a cubic plane. Below we consider the APB in the $L1_2$ lattice contained in the (010) plane. In this case, the observed mesoscopic saw-tooth microstructures are homogeneous along the [001] axis and the saw-tooth pattern is located in the (001) plane. The homogeneity of the heterogeneous microstructure along the [001] axis actually means that there is no diffusion along this axis. Under this condition, the 3D problem of the microstructure is reduced to the 2D problem. The assumption of homogeneity along the [001] direction drastically simplifies the simulation model: it implies that concentration \bar{c} and l.r.o. parameters η_1, η_2, η_3 in all equations of the 3D model do not depend on the coordinate z along the [001] axis, i.e. $\bar{c}(r) = \bar{c}(x, y)$ and $\eta_p = \eta_p(x, y)$, where x and y now designate the coordinates of columns of atoms in the f.c.c. lattice parallel to the [001] direction. The intersection of these columns with the (001) plane generates the square lattice whose parameter is $a_0/2$ (see Fig. 2). Therefore, the 2D position of the atomic columns is $r = \frac{1}{2} a_0(x, y)$, where the coordinates x, y of the columns are integers.

Counting all nearest and next-nearest interactions within a column and between the neighboring columns gives us the following mixing energies between columns:

$$W_{chem}(r - r') = \begin{cases} 2W_2 & \text{if } |r - r'| = 0 \\ 2W_1 & \text{if } |r - r'| = a_0/2 \\ W_1 & \text{if } |r - r'| = a_0/\sqrt{2} \\ W_2 & \text{if } |r - r'| = a_0 \\ 0 & \text{otherwise} \end{cases} \quad (16)$$

where $r' = \frac{1}{2} a_0(x', y')$. As long as the microstructure homogeneity along the [001] axis is maintained, this 2D model is mathematically equivalent to a 3D model with mixing energies, given by equation (16). Because the $L1_2$, $L1_0$ and the f.c.c. solid solution are compatible with this homogeneity condition, the 2D model correctly reproduces the equilibrium structures, the mean field kinetics, and thermodynamics of the 3D model.

3.2. Strain energy

To establish an origin of saw-tooth microstructures and distinguish the role of the different factors

in its formation, we exclude the effect of the elastic moduli anisotropy. As a matter of fact, the elastic anisotropy is not a factor which considerably complicates the computations. However, as it has been shown in our previous paper [7], even the elastically isotropic model predicts the chess-board structure in Co-Pt and other alloys, reproducing with great accuracy the finest features of their microstructure morphology. It is shown below that the elastically isotropic model also correctly predicts the formation of the saw-tooth morphology and its morphologic features with excellent quantitative agreement with the observations. This actually proves that it is the crystallography of the crystal lattice rearrangement (symmetry and the relation between components of the misfit tensor) rather than the elastic moduli anisotropy that is the major factor determining the mechanism of both the saw-tooth and chess-board structures.

Homogeneity along the [001] axis simplifies equations (11), (13) and (14) for the strain-induced driving force. This homogeneity results in vanishing of k_z in all equations involving the strain energy. Therefore, we used $\mathbf{k} = (k_x, k_y, 0)$ and $\mathbf{e} = (e_x, e_y, 0)$ in all equations involving the strain energy because all integration (summation) over k_z is lifted. With this simplification, the assumption of the elastic isotropy, and the stress-free strain (10), the functions $B_{pq}(\mathbf{k}/k)$ defined in equation (11) are:

$$B_{11}(e_x, e_y, 0)$$

$$= \frac{2\mu\epsilon_3^2}{(1-\nu)\eta_0^4} (((1-d_0)e_x^2 - (1+d_0\nu))^2 + (1-\nu^2)d_0^2)$$

$$B_{33}(e_x, e_y, 0) = \frac{2\mu\epsilon_3^2}{(1-\nu)\eta_0^4} (1 + 2\nu d_0 + d_0^2)$$

$$B_{12}(e_x, e_y, 0)$$

$$= \frac{2\mu\epsilon_3^2}{(1-\nu)\eta_0^4} ((1-d_0)^2 e_x^2 \cdot e_y^2 + d_0(1+d_0)(1+\nu))$$

$$B_{13}(e_x, e_y, 0)$$

$$= \frac{2\mu\epsilon_3^2}{(1-\nu)\eta_0^4} ((d_0 + \nu)(1-d_0)e_y^2 + d_0(d_0 + 1) \times (1 + \nu)) \quad (17)$$

where \mathbf{e} is a unit vector, ν and μ are the Poisson ratio and the shear modulus, respectively, and $d_0 = \epsilon_1/\epsilon_3$ is the stress-free strain parameter. The functions $B_{22}(e_x, e_y, 0)$ and $B_{23}(e_x, e_y, 0)$ are obtained from $B_{11}(e_x, e_y, 0)$ and $B_{13}(e_x, e_y, 0)$ in (17) by the simultaneous $1 \leftrightarrow 2$ and $x \leftrightarrow y$ cyclic permutation. Using equation (17) in equation (14) allows us to formulate the closed analytical form of

the strain-induced driving force for arbitrary l.r.o. parameter profiles.

3.3. Master equation

As has been discussed in Section 3.1, there is no diffusion along the [001] direction if the decomposition maintains homogeneity along this direction. Then substitutional diffusion develops between the [001] columns in the f.c.c. lattice and can be described in terms of the 2D diffusion over the primitive square lattice with the $a_0/2$ parameter. Master equation (2) for the diffusion in the f.c.c. lattice is equally accurate for the 2D model of the diffusion in the square lattice if the elementary diffusion events are the nearest-neighbor jumps and the following probabilities for jumps between columns are assumed:

$$L(\mathbf{r} - \mathbf{r}') = \begin{cases} 2f & \text{if } |\mathbf{r} - \mathbf{r}'| = a_0/2 \\ f & \text{if } |\mathbf{r} - \mathbf{r}'| = a_0/\sqrt{2} \\ -12f & \text{if } \mathbf{r} - \mathbf{r}' = 0 \\ 0 & \text{otherwise} \end{cases} \quad (18)$$

where $\mathbf{r} = \frac{1}{2}a_0(x, y)$ and $\mathbf{r}' = \frac{1}{2}a_0(x', y')$ and x, y , and x', y' are integer coordinates, $f = f_0 \exp(-U/(k_B T))$ is the jump frequency between the nearest-neighbor sites of the 3D f.c.c. lattice.

It is convenient to solve equation (1) using the reduced variables and parameters. The reduced time is $t^* = ft$ and the reduced temperature is $T^* = k_B T/W_1$. The strain energy contribution is determined by the dimensionless parameter

$$\chi = \frac{\mu\epsilon_3^2\nu}{W_1\eta_0^4} \quad (19)$$

where ν is the volume per f.c.c. lattice site and χ determines a balance between the strain and "chemical" energy of the alloy.

3.4. Input parameters for Co-Pt alloys

To apply our simulation model to the Co-Pt alloys, we have to estimate the values of the input parameters, using for this the data obtained in the measurements unrelated to the data obtained from the geometry of the microstructure patterns. A choice of the mixing energies should provide the ordering that produces the $L1_2$ and $L1_0$ phases and their two-phase equilibrium. The two-phase concentration range should be of the order of 1 at.% and should be situated near $c_{Co} \sim 0.4$. These are the estimated values that follow from the TEM observations of the Co-Pt alloy at 963 K [2]. At $W_2/W_1 = -0.2$ and $T^* = k_B T/W_1 = 1.125$ at $W_1 > 0$, our model gives the $L1_2$ and $L1_0$ two-phase range which is close to these estimates. It does automatically produce the $L1_2$ and $L1_0$ phases

that coexist in equilibrium within the $0.4215 < \bar{c} < 0.4320$ composition range.

The most important data for the microstructure prediction are the crystal lattice parameters of the phases at different temperatures and compositions. These data determine the strain energy contribution and all specific features of the two-phase microstructure patterns. The crystal lattice parameter data allow us to calculate the strain component ϵ_3 entering χ in equation (19) and the parameter d_0 determining the anisotropy of the function $B_{pq}(e)$ in (17) characterizing the strain-induced interaction between elements of the microstructure.

The crystal lattice parameters that we need to know are the parameter of the f.c.c. disordered phase, $a_{f.c.c.}$, the parameter of the cubic ordered phase, $a(L1_2)$, and the parameters of the tetragonal $L1_0$ phase, c_t and a_t , within the $L1_2 + L1_0$ composition range at the decomposition temperature (at $c_{Co} \sim 0.4$ and $T = 873$ K). Unfortunately, these data are not available for those compositions and temperatures where the observed saw-tooth structure has been formed. Below we assume that $d_0 = \epsilon_1/\epsilon_3 = 0.2$ and $\epsilon_3 = -0.02$. The following consideration indicates that these values provide a reasonable estimate.

Indeed, according to equation (10), the tetragonal ratio c_t/a_t of the $L1_0$ phase within the two-phase region, expressed through the constants $\epsilon_1 = d_0\epsilon_3$ and ϵ_3 , is

$$\frac{c_t}{a_t} = \frac{1 + \epsilon_3}{1 + d_0\epsilon_3}. \quad (20)$$

With $d_0 = 0.2$ and $\epsilon_3 = -0.02$, equation (20) gives $c_t/a_t = 0.984$. This value is consistent with the experimentally observed tetragonalities of the $L1_0$ phase: for example, the observed tetragonality of the $Co_{47.6}Pt_{52.4}$ alloy is $c_t/a_t = 0.973$ [18]. The tetragonality $c_t/a_t = 0.984$ following from the assumed input parameters is closer to unity than the observed tetragonality, $c_t/a_t = 0.973$. However, this deviation is not an indication of a disagreement with observation results: the composition considered in our model, $c_{Co} \sim 0.4$, is farther off from the stoichiometry, $c_{Co} \sim 0.5$, than the composition, $c_{Co} = 0.476$, of the alloy whose parameter is reported in [18], and thus the tetragonality ratio of our alloy is expected to be closer to unity.

The temperature of our TEM study of the saw-tooth structure in Co-Pt alloys was $T = 873$ K. Our choice, $T^* = k_B T/W_1 = 1.125$, providing the proper concentration range of the $L1_2 + L1_0$ field corresponds to this temperature if $W_1/k_B = 776$ K. This value is used in our simulation.

The estimate $W_1/k_B = 776$ K is obtained by balancing the mean field free energies of the two ordered phases. Since the mean field theory is more accurate for ordered phases, this estimate is more reliable than the one obtained from the f.c.c. $\rightarrow L1_0$ order-

disorder transition temperature T_0 . For the transition temperature T_0 , the mean field theory gives $T_0 = 1.375 W_1/k_B$ at $\bar{c} = 0.5$. It results in $W_1/k_B = 798$ K if the experimental value for the transition temperature, $T_0 = 1098$ K, is used. The latter estimate is less reliable than the previous one because the area near the order-disorder transition point is an area of the phase diagram where the mean field theory is least accurate (it usually gives the order-disorder temperature as 20–30% higher than that calculated by more accurate methods). However, it is still in line with the estimate $W_1/k_B = 776$ K. The equilibrium value of the l.r.o. parameter of the $L1_0$ phase within the $L1_2 + L1_0$ region following from our model at $W_1/k_B = 776$ K is $\eta_0 = 0.2685$.

The estimate for the shear modulus of the Co-Pt alloy gives $\mu \sim 70$ GPa (interpolation between the value $\mu = 81$ GPa for pure Co and $\mu = 62.5$ GPa for pure Pt). Using the parameters $\mu \sim 70$ GPa, $\eta_0 = 0.2685$, $\epsilon_3 = -0.02$, $W_1/k_B = 776$ K, $v = a_0^3/4$, $a_0 = 3.8$ Å in (20) gives the estimate for the input parameter χ :

$$\begin{aligned} \chi &= \frac{\mu \epsilon_3^2}{W_1 \eta_0^4} a_0^3/4 \\ &= \frac{70 \times 10^9 (0.02)^2}{776 \times 1.38 \times 10^{-23} \times (0.2685)^4} \frac{(3.8 \times 10^{-10})^3}{4} \approx 7 \end{aligned}$$

Therefore, our input parameters are:

$$d_0 = 0.2, \quad \chi = 7, \quad T^* = 1.125 \quad (21)$$

4. SIMULATION RESULTS

To find the microstructure evolution as a function of time t^* , the non-linear differential equation (1) for $n(x, y, t^*)$ was solved at each point $r^* = (x, y)$ by using the Euler method. A small random field was added to avoid trapping in local minima. The initial occupation probabilities, $n(x, y, t^* = 0)$, were chosen to describe two unrelaxed $L1_2$ antiphase domains with homogeneous composition $\bar{c} = 0.4235$. The APB was initially situated in the (010) plane and its antiphase vector was $\frac{1}{2}[011]$. A simulation box contained 128×128 sites (the [001] columns in the f.c.c. lattice) that form the square lattice with the crystal lattice parameter $a_0/2$. In order to use periodic boundary conditions in all directions, we have introduced two antiphase boundaries associated with opposite translation vectors.

The dependence of $n(x, y, t^*)$ vs time t^* obtained by the numerical solution of the kinetic equation (1) simulates the subsequent stages of the microstructure development in the heterogeneous $L1_2 \rightarrow L1_0 + L1_2$ decomposition developing on the antiphase boundary. The simulation results are shown in Fig. 3. In Fig. 3, the two-phase morphology is characterized by the coarse-grain concentration profile $\bar{c}(x, y)$. This profile is visualized by shades of

gray. The white contrast describes the $L1_0$ phase [greater value of $\bar{c}(x, y)$]. For a comparison, we also presented in Fig. 3(d) the micrographs of our TEM observation of $\text{Co}_{38.5}\text{Pt}_{61.5}$ annealed at 873 K.

Figure 3(a) shows that the APB located along

the (010) plane remains flat, but at $t^* = 100$ they are consumed by the $L1_0$ precipitate. The precipitate is shown by a white contrast. At this point, our simulation results are still similar to those obtained in Refs [1, 5], where no elastic effects are taken into

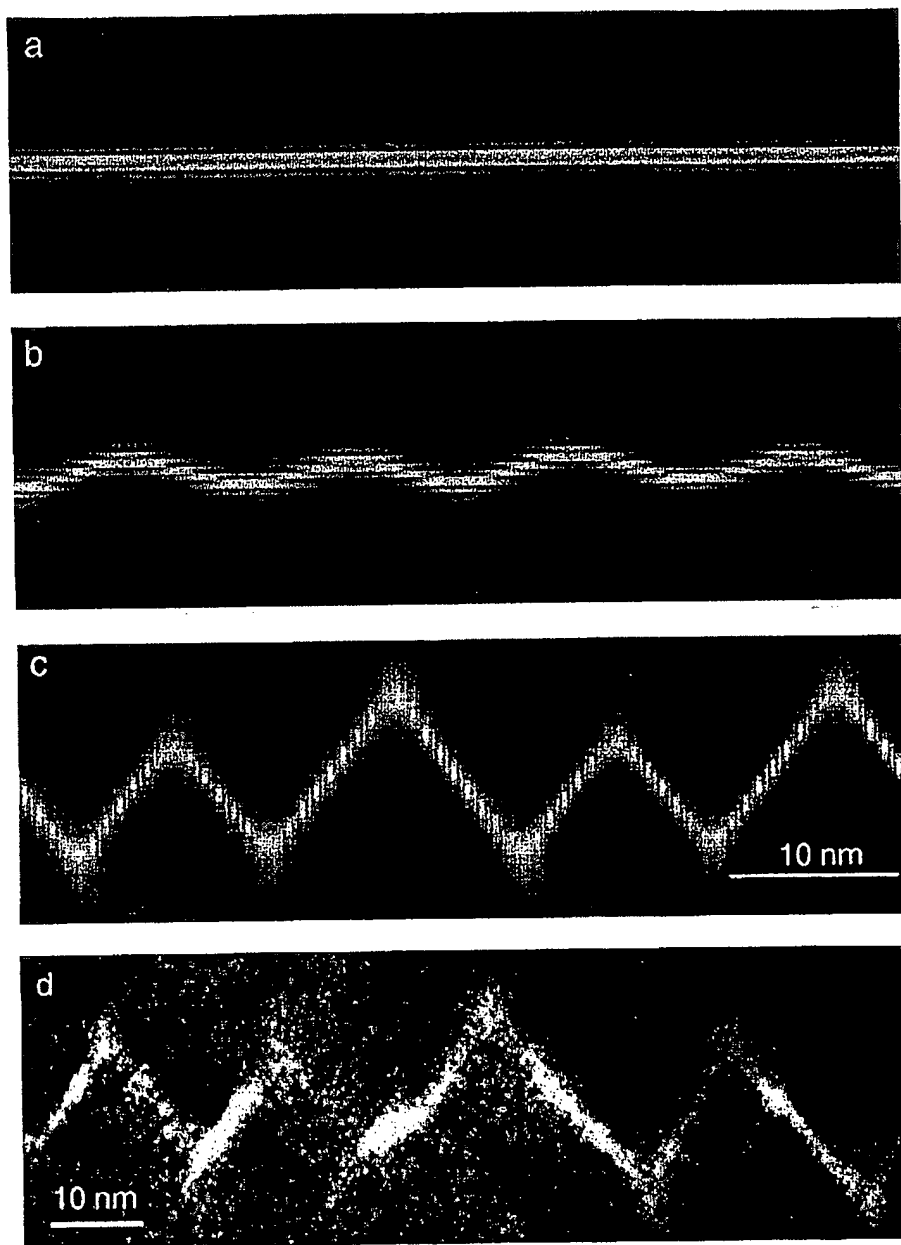


Fig. 3. Comparison between simulation results (a)–(c) and a TEM image of a saw-tooth morphology. The concentration maps (a)–(c) correspond to the reduced times: (a) $t^* = 100$; (b) $t^* = 200$; (c) $t^* = 500$. The dark field image (d) of $\text{Co}_{38.5}\text{Pt}_{61.5}$ was obtained in a zone axis close to (001) with the superstructure reflection (120). The alloy sample was gradually cooled from 1023 to 873 K at the rate of 40 K, aged for 15 days at 873 K and water quenched.

account. The $L1_0$ layer consuming the APB boundary has the (010) habit plane coinciding with the APB plane orientation. The $L1_0$ phase layer has the tetragonal axis parallel to the $[100]$ direction. Therefore, the tetragonal axis is perpendicular to the $\frac{1}{2}[011]$ out-of-phase vector of the APB. This result is in complete agreement with the experimental observations in the Co-Pt system [1, 2].

At $t^* = 300$ [Fig. 3(b)], the situation changes. The precipitate with the (010) habit starts to evolve adopting a wavy shape, which indicates that the $L1_0$ phase plate tends to deviate its habit plane from the (010)_{r.c.c.}

Finally, at $t^* = 500$ [Fig. 3(c)], the $L1_0$ phase forms a saw-tooth morphology. Comparison of Figs 3(c) and (d) illustrates the excellent agreement between our simulation and experimental results for the Co-Pt system.

It is interesting to note the diffuse contrast that is mostly localized around the edges of the saw-tooth. This occurs because the elastic strain around the edges is especially high and deviations of concentration and l.r.o. parameters from their equilibrium values reduce the elastic strain. This phenomenon is illustrated in Fig. 4 where an l.r.o. parameter profile in a $[010]$ direction is presented. This profile intersects a tip of the saw-tooth morphology obtained when $t^* = 500$. In the bulk of the $L1_2$ domains, the three components of the l.r.o. parameter are not strictly equal (in absolute value) as they should be in the absence of the strain field generating the saw-tooth. Furthermore, the value of the second component of the $L1_0$ structure is lower than the stress-free value $\eta = 0.2628$.

5. DISCUSSION

Figure 3 shows that our simulation results are in excellent agreement with the TEM observations [1, 2] of the $Co_{38.5}Pt_{61.5}$ alloy. The simulation indi-

cates that the nucleation of the $L1_0$ phase occurs by the heterogeneous mechanism. The tetragonal $L1_0$ phase forms at APBs as a single-domain layer that gradually consumes the APB [Fig. 3(a)]. The tetragonal axis of this layer is perpendicular to the antiphase shift vector of the APB. The antiphase shift $a_0[0\frac{1}{2}\frac{1}{2}]$ for the (010) APB resulted in the formation of the domain of the $L1_0$ phase whose tetragonality axis is parallel to the $[100]$. Such domains will be called x-domains. The (010) plate of the $L1_0$ phase [white strip on Fig. 3(a)] is not stable. It evolves into a saw-tooth structure formed by alternating plates of x-domains with different habit planes [Figs 3(b) and (c)]. This is also in an agreement with the TEM observations [1, 2].

It should be emphasized that practically no constraints were imposed on the system to choose the optimal transformation path from its initial state of two $L1_2$ antiphase domains separated by sharp unrelaxed APB. The entire evolution path illustrated by Figs 3(a)–(c) is fully determined by the kinetic equation (1).

The simulated microstructure shows not only qualitative but also excellent quantitative agreement with the TEM observations of the $Co_{38.5}Pt_{61.5}$ alloy. In the simulated picture [Fig. 3(c)], the angle between the normals to the tooth surfaces (between the habit planes of the x-domain plates forming a "tooth" of the structure) and their tetragonal axis directions is about 35° . This angle coincides with the one observed in the TEM pictures [Fig. 3(d)].

In the simulation, the microstructure evolution is practically stopped when the structure shown in Fig. 3(c) forms. The typical size of a "tooth" obtained at this stage is about 10 nm. A similar size is observed in the TEM picture after 15 days of aging of the $Co_{38.5}Pt_{61.5}$ alloy at 873 K [Fig. 3(d)]. Therefore, the scale of the simulated saw-tooth microstructure is in agreement with the TEM observations [compare Figs 3(c) and 3(d)].

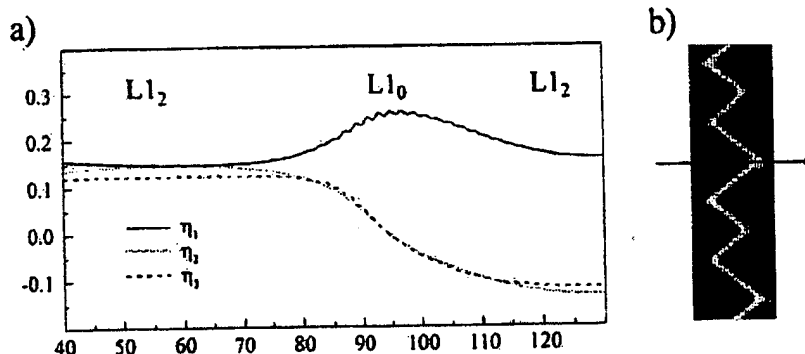


Fig. 4. (a) l.r.o. profile along $[010]$ intersecting a tip of the saw-tooth morphology when $t^* = 500$. The $L1_2$ domains of the type $\eta[111]$ and $\eta[1\bar{1}\bar{1}]$ are separated by a zone of $L1_0$ structure of the type $\eta_0[100]$. The path corresponding to the l.r.o. profile (a) is sketched by an arrow in (b).

The most challenging part of the theoretical characterization of the system is the accurate determination of the transformation kinetics in real time. The real time t is related to the reduced time t^* of our simulation by equation

$$t = t^* / f = t^* / (f_0 \exp(-U/(k_B T))) = 1/f_0 \exp(U/(k_B T)) t^* \quad (22)$$

The coefficient relating real and reduced time in (22) is very sensitive to the activation energy of diffusion U and the aging temperature T . Besides, the accurate data on the diffusion coefficients at the composition of the simulated Co-Pt alloy are not available. To estimate the value of U , we have used the activation energy $U = 279.3$ kJ/mol for diffusion of Pt in Co [19]. The typical number of "attempts" f_0 for a diffusional jump is of the order of a typical frequency of the crystal lattice vibration, $f_0 \sim 10^{13}$ s⁻¹. Using these values in (22) for $t^* = 500$ at $T = 873$ K gives $t \sim 2.5 \times 10^6$ s = 30 days. The TEM picture of the saw-tooth structure shown in Fig. 3(d) was obtained by gradual cooling of Co_{38.5}Pt_{61.5} from 1023 to 873 K at the rate of 40 K, followed by aging for 15 days at 873 K. Given the fact that (i) the alloy has already been partially transformed during gradual cooling prior to aging at 873 K and (ii) the input data for this estimate are very approximate, the estimated structure formation time, 30 days, is in reasonable agreement with the 15 days of aging time in the real system. In cases like this, an agreement that is better than an order of magnitude can hardly be expected.

All input parameters that are used in the simulation can be found from independent measurements of the crystal lattice parameters and the phase diagram, i.e. from the data unrelated to the morphology of the microstructure. The simulated structures are sensitive to the crystal lattice misfit data, which determine the crystallographic parameter $d_0 = c_1/c_2$ and reflects the geometry of the crystal lattice rearrangement in the phase transformation. The crystal lattice misfit determines the magnitude and spatial anisotropy of this strain. The sensitivity of the microstructure to the crystallographic misfit data follows from the fact that the long-range strain is a major factor determining the morphology of the mesoscopic microstructure.

The geometry of the microstructure is much less sensitive to the parameter χ weighting the contribution of the strain energy with respect to the "chemical" energy. The simulation is also not very sensitive to the choice of the parameters $W(r)/(k_B T)$, as long as this choice produces the L1₂ and L1₀ ordering and the correct two-phase range at the simulation temperature.

As is known, the mean field approximation underestimates the contribution of the atomic correlations to the alloy thermodynamics, especially for

the disordered state. Although the simulated microstructures in this study are obtained by the solution of the mean field version of the ME, the agreement between the simulated microstructures and the TEM observations is excellent. The latter indicates that the accuracy in the strain energy treatment here is much more important than an underestimation of atomic correlation. It also shows that the KS theory is well suited to treat the strain energy contribution.

The second reason why the mean field ME proves to be sufficient to describe this system is that inaccuracy of the mean field approximation is partially compensated by a choice of the "chemical" energies W_1 , W_2 as fitting parameters to the observed phase diagram. Besides, as is well known, the higher the l.r.o., the more accurate becomes the mean field approximation (it becomes exact at 0 K where the l.r.o. reaches the maximum possible values). The latter is also a factor since we consider the processes where all phases are always in the ordered state where the higher accuracy of the mean field theory should be also expected.

The simulation results shown in Figs 3(a)-(c) demonstrate details of the saw-tooth structure formation. The formation mechanism can be qualitatively explained by the combined effect of the APB and transformation strain. The APBs in the L1₂ phase are high-energy defects. Thus, the free energy decrease due to the transformation of APBs into the L1₀ phase is greater than it would be if the L1₀ phase was formed in the bulk of the L1₂ parent phase. In this situation the L1₀ phase forms by the heterogeneous nucleation and the APBs are the nucleation sites. The L1₀ phase formed on the APBs consumes them, replacing the APBs by a single-domain layer. The initial orientation of this newly formed L1₀ phase layer inherits the orientation of the APB, which is the (010) plane in our case. This situation is reproduced by the computer simulation [Fig. 3(a)]. However, the (010) orientation is not a strain energy minimizer and thus is not stable. The strain energy minimum is achieved if the normal e_1 to a plate of the L1₀ phase "rotates" from its initial direction $e_{1(010)}$ normal to (010) to either $e_1 = (\cos 35^\circ, +\sin 35^\circ, 0)$ or $e_2 = (\cos 35^\circ, -\sin 35^\circ, 0)$ directions. The L1₀ plates with both types of habit planes, normal to e_1 and e_2 , have the same strain energy.

However, this habit plane rotation occurs only if the decrease in the strain energy outweighs the increase in the interfacial energy due to a deviation of the interface from the minimum interfacial energy orientation [9]. It does not occur for thin plates since the interfacial energy of thin plates plays the dominant role. Thus, the plate is parallel to the plane of the minimum interfacial energy. In our case, the minimum interfacial energy plane is the (010) plane parallel to the APB. When the thickness D of the plate exceeds the critical value

D_{cr} during the growth process, the bulk strain energy becomes more important than the interfacial energy and the plate starts to rotate to either of two orientations dictated by the bulk energy minimum. A balance between strain and interfacial energies of the plate [9] results in the following criterion for the critical thickness:

$$D_{cr} = \frac{4\Delta\gamma}{|\Delta B|}$$

where $\Delta B = [B_{11}(e_1) - B_{11}(e_{010})] < 0$ and $\Delta\gamma = [\gamma(e_1) - \gamma(e_{010})] > 0$, $\gamma(e)$ is the $L1_0/L1_2$ interfacial energy of the interface normal to the unit vector e . If the thickness D of the $L1_0$ interfacial layer is less than D_{cr} , the layer just replaces the $L1_2$ antiphase domains and has the (010) habit. During the growth, when the thickness D exceeds D_{cr} , these plates start to deform forming the saw-tooth structure. The teeth of the saw-tooth structure is comprised of the plates of the $L1_0$ phase, which determine a shape of teeth. Points where the nearest plates join are the tooth tips. This transformation process is illustrated by Figs 3(a)–(c). The TEM observations fully agree with these conclusions. According to observation [1, 2], the smooth wetting layers of the $L1_0$ phase separating the $L1_2$ phase antiphase domains transform into the saw-tooth structure when the thickness of the layers exceeds 3–4 nm.

In fact, the qualitative consideration presented above explains only why the $L1_0$ phase plates rotate so that their habit is normal to either e_1 or e_2 vectors when the thickness of the plates exceeds the critical value. This is not sufficient to explain why these plates rotate to self-assemble themselves in the continuous saw-tooth zig-zag pattern. The latter can be understood if we take into account that the rotations of the elements of a single (010) $L1_0$ domain plate [Fig. 3(a)] into a set of the $L1_0$ plates with the different habits should occur by maintaining the continuity of this domain. This continuity of the domain is required to prevent a formation of new $L1_0/L1_2$ boundaries on the edges of each plates, since the formation of edges would raise both interfacial and strain energies. It is an attachment of these plate edges that produces the continuity of the $L1_0$ domain, which results in the formation of the saw-tooth structure.

Eventual freezing of the saw-tooth structure is a result of extreme difficulties in the coarsening after the growth stage is completed. Indeed, the geometry of the saw-tooth structure is such that its coarsening, which maintains the $L1_0$ phase continuity and orientations of the $L1_0$ plates forming the zig-zag pattern, would require a collective microstructure reconstruction. This process would involve simultaneous and synchronic evolution of several neighboring plates of different orientations, i.e. the process that is much slower than the conventional

Ostwald ripening of separate particles. Freezing of the microstructure evolution observed in our simulation after the time period $t^* \sim 500$ is consistent with this conclusion.

Finally, it is very interesting that our simulation indicates that the concentration and order parameters deviate from the equilibrium stress-free values to lower the misfit between the $L1_0$ layer and the $L1_2$ matrix (Fig. 4). In fact, the precise values of the l.r.o. parameter and the concentration under the elastically constrained condition depend on the microstructure, and cannot be inferred in advance. This effect cannot be predicted by using the sharp boundary approximation that usually neglects the freedom for the system to relax the l.r.o. parameter and concentration profiles from their equilibrium values to reduce interfacial and the strain energies. An advantage of the field methods is that they do not impose any a priori constraint on the way the system balances the different contributions to the total free energy.

6. SUMMARY

This work presents the first microscopic kinetic model which describes the major structural characteristics of the decomposition in the $L1_2 + L1_0$ stability region of the f.c.c. binary alloy. The proposed theory and the computer simulation explain the mechanism of the saw-tooth structure formation in the Co–Pt generic system and provide insight into the conditions where this structure can be expected. The saw-tooth structure is formed within the $L1_0 + L1_2$ area near the solubility line of the $L1_2$ phase due to the transformation strain accommodation.

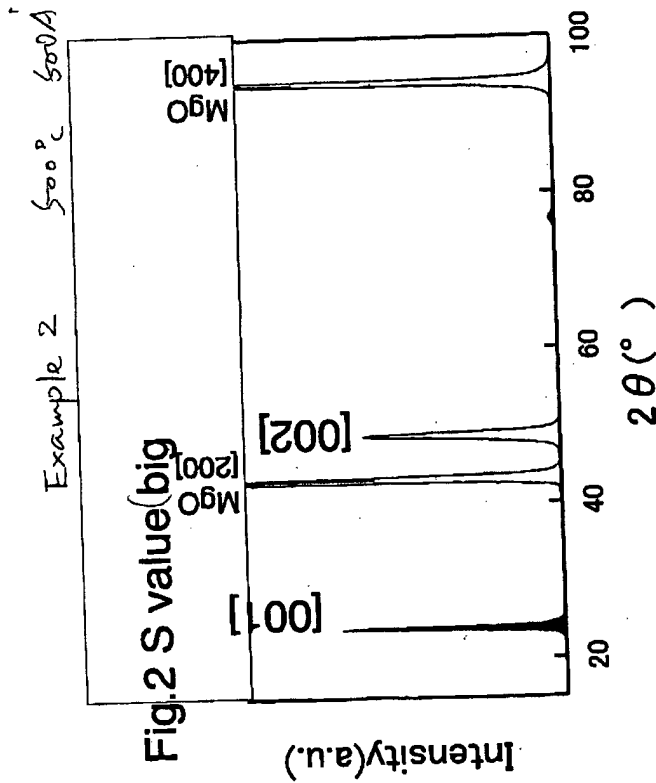
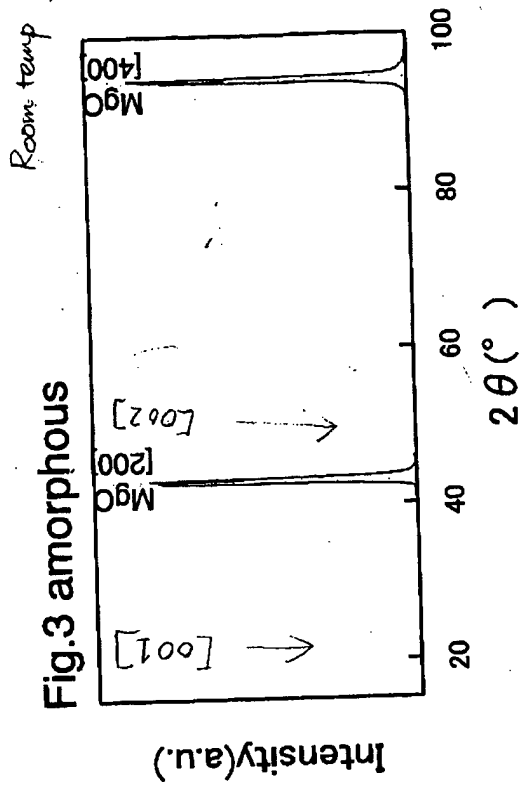
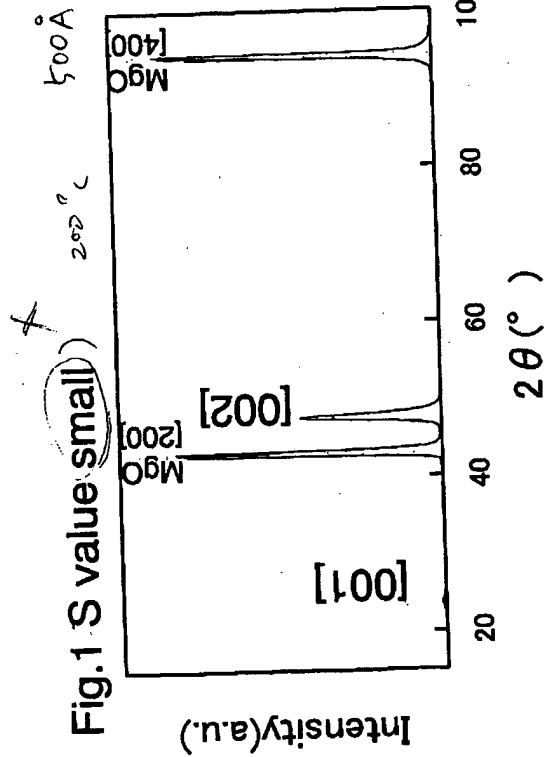
The model predicts that the $L1_2 \rightarrow L1_0$ transformation starts from a formation of $L1_0$ phase layers wetting the APBs. In agreement with the TEM observations, the tetragonal axis of the $L1_0$ structure is normal to the antiphase vector. When the thickness of a layer reaches about 3–4 nm, our model predicts the formation of the saw-tooth microstructures. The saw-tooth structure does not alter the global orientation of the APB but drastically reduces the strain energy by a local reorientation of the $L1_0$ phase layers along the elastically soft directions.

The simulation study demonstrates the ability of the model to provide excellent quantitative agreement with the TEM observations.

Acknowledgements—We are grateful to Dr A. Loiseau for her help in obtaining the TEM pictures and to Drs A. Finel and F. Ducastelle for valuable discussions. We gratefully acknowledge the financial support of the National Science Foundation under grant no. DMR 98 17235. The simulations were performed at the Pittsburgh Supercomputing Center under grant no. DMR 93-0013P.

REFERENCES

1. Le Bouar, Y., Ph.D. thesis, Ecole Polytechnique, France, 1998.
2. Leroux, C., Loiseau, A., Broddin, D. and Van Tendeloo, G., *Phil. Mag. B*, 1991, 64(1).
3. Cheong, B., Hono, K. and Laughlin, D. E., *Acta metall. mater.*, 1994, 42(7), 2387.
4. Wang, Y. and Khachaturyan, A. G., *Phil. Mag. A*, 1995, 72, 1161.
5. Le Bouar, Y., Loiseau, A., Finel, A. and Ducastelle, F., *Phys. Rev. B*, 2000, 61, 3317.
6. Udob, K.-I., El Araby, E. M., Tanaka, Y., Hisatsune, K., Yasuda, K., Van Tendeloo, G. and Van Landuyt, J., *Mater. Sci. Eng.*, 1995, A203, 164.
7. Le Bouar, Y., Loiseau, A. and Khachaturyan, A. G., *Acta mater.*, 1998, 46(8), 2777.
8. Khachaturyan, A. G., *Sov. Phys. Solid State*, 1968, 9, 2040.
9. Khachaturyan, A. G., *Theory of Structural Transformations in Solids*. Wiley, New York, 1983.
10. Chen, L.-Q. and Khachaturyan, A. G., *Acta metall. mater.*, 1991, 39(11), 2533.
11. Gouyet, J. F., *Europhys. Lett.*, 1993, 21(3), 335.
12. Martin, G., *Phys. Rev. B*, 1990, 41(4), 2279.
13. Martin, G. and Soisson, F., in *Solid-Solid Phase Transformations*, ed. W. C. Johnson, J. M. Howe, D. E. Laughlin and W. A. Sofka. The Minerals, Metals & Materials Society, 1994.
14. Khachaturyan, A. G., *Prog. Mater. Sci.*, 1978, 22.
15. Khachaturyan, A. G. and Shatalov, G. A., *Sov. Phys.-Solid State*, 1969, 11, 118.
16. Chen, L.-Q., Wang, Y. and Khachaturyan, A. G., *Phil. Mag. Lett.*, 1992, 65(1), 15.
17. Wang, Y., Chen, L.-Q. and Khachaturyan, A. G., *J. Am. Ceram. Soc.*, 1993, 76, 3029.
18. Newkirk, J. B., Smoluchowski, R., Geisler, A. H. and Martin, D. I., *J. Appl. Phys.*, 1951, 22, 290.
19. Landolt-Börnstein, Numerical Data and Functional Relationship in Science and Technology, in *Diffusion in Solids Metals and Alloys*, Vol. 26, ed. H. Ullmann. Springer-Verlag, Berlin, 1990.



BEST AVAILABLE COPY